Edge displacement scores

Arne Melsom[1]

[1]Norwegian Meteorological Institute

Correspondence: Arne Melsom (arne.melsom@met.no)

Abstract. As a consequence of a diminishing sea ice cover in the Arctic, activity is on the rise. The position of the sea ice edge, which is generally taken to define the extent of the ice cover, changes in response to dynamic and thermodynamic processes. Forecasts for sea ice expansion on synoptic time scales due to an advancing ice edge will provide information that can be of significance for open ocean operations in polar regions. However, the value of this information depends on the quality of the forecasts. Here, we present methods for examining the quality of forecasted sea ice expansion on sub-seasonal time scales and the geographic location where the largest expansion are expected from the forecast results. The algorithm is simple to implement, and an examination of two years of model results and accompanying observations demonstrates the usefulness of the analysis.

1 Introduction

Due to climate change the sea ice extent is in decline in the Arctic (Parkinson, 2014). This change has led to increased activity in the region, and commercial shipping in open waters via Arctic sea routes will become increasingly economically viable in the 21st century (Aksenov et al., 2017). Thus, ~~products~~ data sets for monitoring and forecasting sea ice conditions are receiving growing attention.

The past years have seen a flurry of activity related to assessing the quality of sea ice ~~products. Dukhovskoy et al. (2015) present~~ data sets. Dukhovskoy et al. (2015) presented a review and comparison of various traditional metrics for assessments of the skill of sea ice models. Goessling et al. (2016) ~~introduce~~ introduced the Integrated Ice-Edge Error (IIEE), a quantity for describing mismatching sea ice extents from two ~~products~~data sets, in their examination of the predictability of the sea ice edge. Melsom et al. (2019) took advantage of the IIEE in their examination of various metrics for assessment of the quality of forecasts for the sea ice edge position. Methods for examining the quality of probabilistic results for sea ice conditions have been introduced by Goessling and Jung (2018) and Palerme et al. (2019). Recently, Cheng et al. (2020) ~~have~~ examined the accuracy of a visually estimated ice concentrations monitoring product.

The changing position of the sea ice edge is generally not only shifted by dynamic advection, but can be significantly affected by the thermodynamics as well (Bitz et al., 2005). Thus, the temporal displacement of the sea ice edge will be affected by freezing along the perimeter of the sea ice extent in winter, and melting in summer. Hence, pattern-recognition algorithms for displacements using maximum cross-correlation (MCC) methods such as those introduced by Leese et al. (1971) for wind vectors, and later for ocean surface currents (Tokmakian et al., 1990) and sea ice vectors (Lavergne et al., 2010), are not ideal for tracking displacements of the sea ice edge.

Ebert and McBride (2000) examined the position error of the contiguous rain area in weather forecasts. They determined the error vector from a total squared error minimization method when shifting the forecasted rain region to match the corresponding observations. Their preference of applying an error minimization algorithm rather than an MCC approach was motivated by the former having better representations of displacement of rainfall maxima. An object-based approach with a focus on assessing the quality of forecasts for highly localized and episodic phenomena was introduced by Davis et al. (2006). Like in Ebert and McBride (2000), their focus when evaluating displacement is on the objects' centroid. Displacement of the perimeter of the contiguous rain area was not addressed in ~~their~~ either investigation.

We begin this study by presenting a new algorithm for assessing the quality of representations of the sea ice edge by comparing results for two different ~~products. This is~~ data sets. We examine displacements over time of the sea-ice edge, and compare model results for displacement distances versus observed displacements. The methods that are applied to this end are described in Sect. 2~~, where issues related to sea ice emerging in the vicinity of boundaries are also addressed. Next, in~~ . In Sect. 3 we apply the algorithm in an examination of displacements of the sea ice edge in the Barents Sea~~in a model product, and compare the results to data from an observational product~~. Finally, we provide our concluding remarks in Sect. 4. Details and extensions are provided in two appendices.

2 Methods

In order to illustrate the validation metrics that are introduced in this ~~Sect., some idealized distributions are~~ section, a set of idealized ice edges is introduced, as depicted in Fig. 1. The domain is divided into 1000×500 square grid cells, and we set the length of the side of a grid cell to 1. Denote the line that separates regions with binary values 0 and 1 as an edge line, and let ~~$L^{(o)}(t)$ and $L^{(m)}(t)$~~ $L^O(t)$ and $L^M(t)$ denote observed and modeled edges, respectively, at time t. Idealized examples with edges for ~~$L^{(o)}$ and $L^{(m)}$~~ L^O and L^M at two different times, t_0 and $t_0 + \Delta t$, are displayed. In the context of forecasting, ~~$L^{(m)}(t_0)$~~ $L^M(t_0)$ may be taken to represent the model initialization at t_0 and ~~$L^{(m)}(t_0 + \Delta t)$~~ $L^M(t_0 + \Delta t)$ is then the forecast at a temporal range of Δt. The other binary fields can represent observations at the same times. This configuration sets us up for introducing validation metrics for how the sea ice edge becomes displaced over time, and how model results and observations for such temporal evolutions compare.

2.1 ~~Single product~~ Validation metrics for ice edge displacement in one data set

We aim at defining metrics that describe differences in maximum sea ice expansion from sea ice edge displacements between two ~~products~~data sets. In order to do so, we must first introduce a quantity that properly measures the maximum displacement

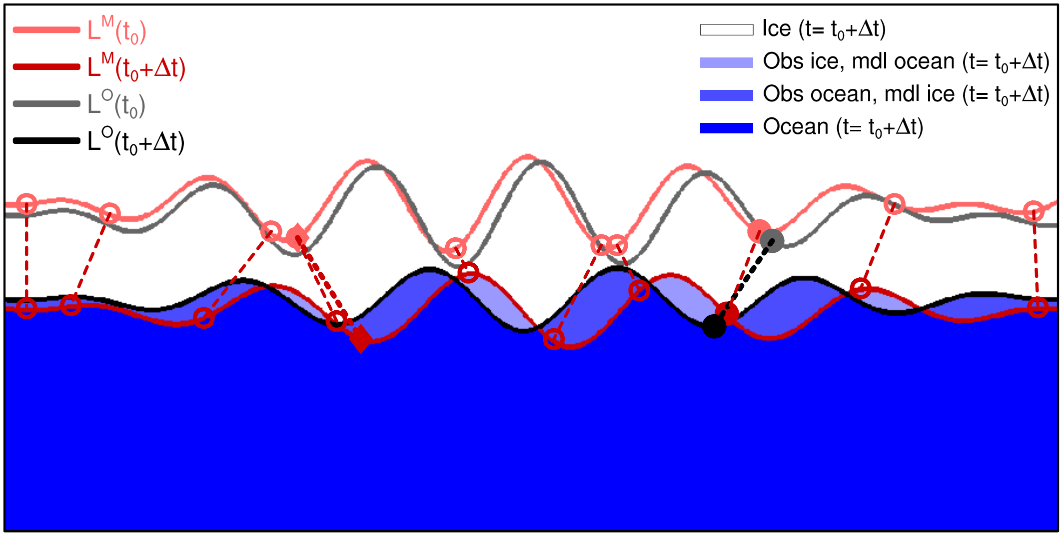

Figure 1. Binary fields with values of 1 (ice) and 0 (no ice/ocean) are displayed by white and blue color shading, respectively. Light shades of blue indicate regions with a non-overlapping ice cover, as indicated by the ~~inset~~ color legend. The derived modeled and observed ice edges ~~$L^{(m)}$~~ L^{M} and ~~$L^{(o)}$~~ L^{O} at t=t_0+Δt are drawn as red and black lines, respectively. The corresponding ice edges that are taken to represent the situation at t_0 are drawn as light red and gray ~~curves~~lines. The full black circle indicates the position on the observed ice edge at t_0+Δt which has the largest distance to the ice edge at t_0 ~~, shown by~~ (the full gray circle). The largest displacement of the model ice edge is marked by full diamonds. The full red circle is the position along the model ice edge at t=t_0+Δt closest to the full black circle, while the full light red circle is the position of the observed ice edge at t_0 closest to the full red circle. All dashed lines represents displacements as defined by Eq. (3). Open circles indicate a random selection of displacement positions for the model results, see the text for details.

in one ~~product~~data set. Here a definition is provided which is a gridded, signed, one-sided variation of the Hausdorff distance (Dukhovskoy et al., 2015).

For the remainder of this investigation we will take the binary fields to be representations of sea ice, with values assigned to 0 and 1 for conditions of no ice and ice, respectively. We will here associate the presence of ice (value 1) with sea ice concentration c exceeding $c_{edge} = 0.15$. In a gridded representation the ice edge can then be taken to be constituted by the grid cells $e = [i,j]$ that meet the condition

$$c[i,j] \geq c_{edge} \quad \wedge \quad \min\left(c[i-1,j], c[i+1,j], c[i,j-1], c[i,j+1]\right) < c_{edge} \tag{1}$$

where $\wedge$ is the logical AND operator. Denoting the ~~N~~ $N(t)$ grid cells that satisfy this condition ~~by $e_1, e_2, \ldots, e_N$~~ for time t by $e_1^{(t)}, e_2^{(t)}, \ldots, e_N^{(t)}$ the ice edge for time t is then the line

$$L(t) = \{e_1{}^{(t)}, e_2{}^{(t)}, \ldots, e_{\cancel{N}\,N(t)}{}^{(t)}\} \tag{2}$$

This follows the algorithm presented in Melsom et al. (2019). Let ~~$L^{(1)}, L^{(2)}$~~ $L(t_0), L(t_0+\Delta t)$ denote the sea ice edges ~~for two representations of the sea ice cover~~at times t_0 and $t_0+\Delta t$, respectively. Furthermore, let ~~$d_n^{2:1}$~~ $d_n^{\Delta t}$ be the displacement distance between grid node $e_n^{(2)}$ in $L^{(2)}$ and line $L^{(1)}$ a grid cell $e_n^{(t_0+\Delta t)}$ in $L(t_0+\Delta t)$ and line $L(t_0)$, *i.e.*,

$$d_n{}^{2:1\,\Delta t} = s_n \min ||e_n{}^{(2)\,(t_0+\Delta t)} - L^{(1)}(t_0)|| \tag{3}$$

where s Here, $||z||$ is the Euclidean distance of z and the minimum is considered for the distances between grid cell $e_n^{(t_0+\Delta t)}$ and each of the grid cells belonging to $L(t_0)$. Furthermore, s_n is +1 or -1 when $e_n^{(2)}$ $e_n^{(t_0+\Delta t)}$ is on the no ice or ice side of $L^{(1)}$ $L(t_0)$, respectively, i.e. , s is +1 if $c[e_n^{(2)}]^{(1)} < c_{edge}$ and -1 if $c[e_n^{(2)}]^{(1)} \geq c_{edge}$ ($c[e]^{(1)}$ is as explicitly defined by Eq. 4 below. The length of dashed lines in Fig. 1 correspond to the displacements $\min ||e_n^{(t_0+\Delta t)} - L(t_0)||$ for selected cells $e_n^{(t_0+\Delta t)}$.

If we denote the sea ice concentration for grid cell e for the representation with an ice edge given by $L^{(1)}$) . Here, $||z||$ is the Euclidean distance of z. at the time t_0 for a grid cell $e_n^{(t_0+\Delta t)}$ (belonging to the ice edge at $t_0+\Delta t$) by $c[e_n^{(t_0+\Delta t)}](t_0)$, s_n is given as follows:

$$s_n = \begin{cases} -1 & \text{if } c[e_n^{(t_0+\Delta t)}](t_0) \geq c_{edge} \\ +1 & \text{if } c[e_n^{(t_0+\Delta t)}](t_0) < c_{edge} \end{cases} \tag{4}$$

We can now introduce the maximum distance as expansion displacement as

$$d_{max}{}^{2:1\,\Delta t} = \max(d_n{}^{2:1\,\Delta t}) \quad , \quad n = 1, 2, \ldots, N(t_0+\Delta t) \tag{5}$$

Note that the definition of the sign s in Eq. (3) has been chosen so that Eq. (5) will return the largest positive value among $d_n^{2:1}$ $d_n^{\Delta t}$. If all values of $d_n^{2:1}$ $d_n^{\Delta t}$ are negative, the result is the negative value distance with the lowest magnitude. The definition of s was designed so that $d_{max}^{2:1}$ $d_{max}^{\Delta t}$ will represent the displacement of the largest sea ice advance from $L^{(1)}$ to $L^{(2)}$. For reference $L(t_0)$ to $L(t_0+\Delta t)$.

If we briefly introduce $d_m^{-\Delta t}$ as the shortest distance from a grid cell e_m of $L(t_0)$ to the line $L(t_0+\Delta t)$, we note that the Hausdorff distance d_H between lines $L^{(2)}$ and $L^{(1)}$ is $L(t_0+\Delta t)$ and $L(t_0)$ is

$$d_H = max(|d_n{}^{2:1\,\Delta t}|, |d_m{}^{1:2\,-\Delta t}|) \tag{6}$$

see e.g. Dukhovskoy et al. (2015).

model results observations 0 20 0 0.08 20 40 0.05 0.14 40 60 0.15 0.15 60 80 0.13 0.43 80 100 0.51 0.20 100 120 0.17 0 Category distribution of displacement distances computed from Eq. (5), with $L^{(2)} = L^{(m,o)}(t_0+\Delta t)$ and $L^{(1)} = L^{(m,o)}(t_0)$ as displayed in Fig. 1, respectively.

So far, we have restricted the analysis to consider the maximum displacement. However, it is of interest to examine more generally the displacement distance between $L^{(2)}$ and $L^{(1)}$. In addition to a visual inspection that can be done by looking at a graphical presentation (see Fig. 1 for examples), we can consider all values for $d_n^{2:1}$ and summarize the distribution in a table with a suitable definition of distance categories, or present the distribution as e.g. a cumulative probability distribution. The distribution of selected distance categories for the idealized model results displayed For the various quantities we reference

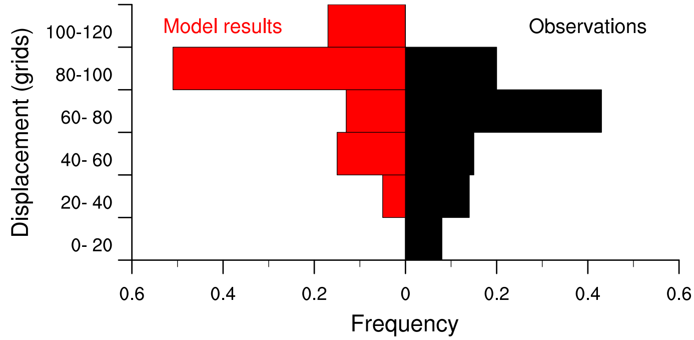

Figure 2. Histograms for the distribution of displacement distances computed from Eq. (5) for the ice edges displayed in Fig. 1. The mean displacement distances for model results and observations were 82 grids and 61 grids, respectively.

model results and observations by superscripts M and O. For the set of binary fields depicted in Fig. 1~~is given in Table ??. We find that in this case, $d_{max}^{m(t_0+\Delta t):m(t_0)} = 113.2$~~, we find that $d_{max}^{M;\Delta t} = 113.2$ (the distance between the red and light red diamonds in the figure), while ~~$d_{max}^{o(t_0+\Delta t):o(t_0)} = 97.9$~~ $d_{max}^{O;\Delta t} = 97.9$ (the distance between the black and gray full circles).

The maximum distance in Eq. (5) provides a single measure to examine the ice-edge displacement. However, it can be more informative to analyze the whole distribution of the displacements $d_n^{\Delta t}$ defined by Eq. (3), rather than their maximum only. This can be done by inspecting a histogram of the displacements $d_n^{\Delta t}$ (Fig. 2). Another option is to present the cumulative probability distribution of $d_n^{\Delta t}$ (Fig. 3).

To avoid inflating the sample size~~when time series results are examined~~, one may consider subsampling at the spatial decorrelation length along the ice edge. For the distribution of ~~$d_n^{2:1}$~~ $d_n^{\Delta t}$ a proper decorrelation length can be computed if the edge ~~nodes $e_n^{(2)}$~~ cells $e_n^{(t_0+\Delta t)}$ are in sequence along ~~$L^{(2)}$.~~

~~Also, when~~ $L(t_0+\Delta t)$. A detailed description for this procedure is given in Appendix A. Furthermore, when subsampled results are inspected, a time series ~~of results is examined,~~ for the distribution of ~~$d_{max}^{2:1}(t)$~~ $d_{max}^{\Delta t}(t)$ can be examined analogously to results for ~~$d_n^{2:1}$~~ $d_n^{\Delta t}$. We will show results for ~~$d_{max}^{2:1}(t)$~~ $d_{max}^{\Delta t}(t)$ when comparing model results and observations in ~~the case study that is undertaken~~ Sect. 3.2.

Sea ice data sets may be regional, having one or more boundaries along which the domain is connected to the surrounding area along open ocean boundaries. In that case, sea ice may be advected into the domain under consideration across an open boundary, and the algorithm presented above should be modified in order to avoid misinterpretations of results for displacement distances. Such modifications are introduced in Appendix B. An illustrative situation will be discussed in Sect. ~~3~~3.2.

Finally, note that all of the expressions above may be extended and used for analysis of distances between any two lines that both form perimeters of binary fields.

2.2 ~~Two-product metrics~~Comparison of the displacements of modeled and observed ice edges

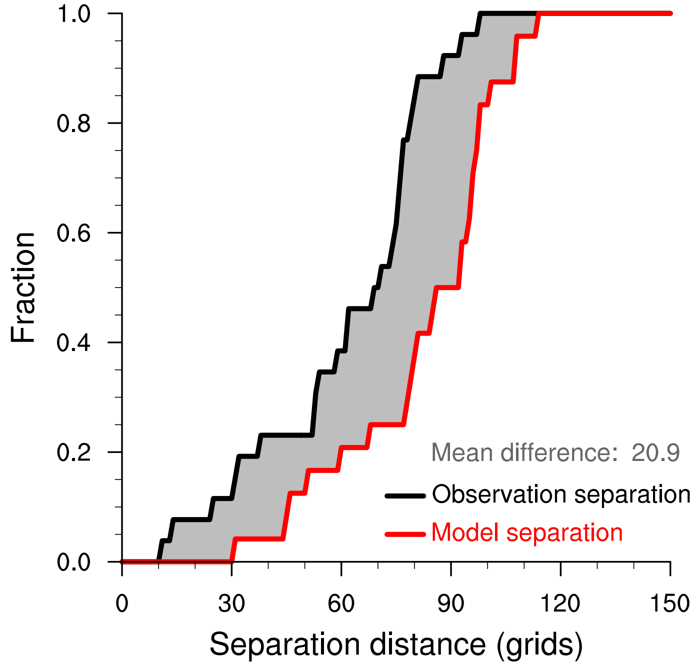

Figure 3. Cumulative distributions of the separation (ice edge displacement) distances from t_0 to ~~$t_0 + \Delta t$~~$t_0 + \Delta t$, for model results (red line) and observations (black line). Shown here are results for the idealized example ~~, as~~ displayed in Fig. 1, with distances subsampled at intervals of the decorrelation lengths, which are 42 and 38 grid cells along the ice edge for the model results and observations, respectively. The mean separation distance difference for the present subsample of ice edge grid cells is the integral of the area between the ~~curves~~lines, here displayed by gray shading. In this case, the mean difference is 20.9 in grid cell units, with larger displacement values in model results than from observations.

~~The main purpose of the work presented here is to define metrics that can contribute in an evaluation of the quality of model forecasts when complementary observations are available. Consequently~~In the previous section we focused on metrics which describe the displacement of a single (modeled or observed) sea ice edge. In this section we extend these to assess the differences in the displacements of the modeled versus observed ice edge. For this purpose, binary fields that are taken to represent observations as well as model results are introduced, as displayed in Fig. 1.

~~A useful initial evaluation of how~~ We start the comparison of model results for displacement and the corresponding observational data ~~compare, is to~~ by inspecting their cumulative distributions. For the idealized set of ice edges considered here, the distributions of ice edge displacement distances are displayed in Fig. 3. The shapes of the cumulative distributions are similar, with model displacements shifted approximately 20 grid units higher for the entire distribution.

We aim to compare model results for displacement distances with the corresponding displacements from observational data. First, we inspect their cumulative distributions ~~. These distributions~~ which are displayed for the idealized example in Fig.s 2 and 3. We note that the shapes of the cumulative distributions in Fig. 3 are similar, with model displacements shifted approximately 20 grid units higher for the entire distribution.

From the perspective of an observer, a useful ~~property~~ attribute is the quality of the forecasted maximum displacement of the binary field, over the forecast period. A simple ~~quantity that provides relevant information ,~~ metric which provides this type of information is the difference in the maximum displacement as given by Eq. (5), *i.e.*,

$$\Delta d_{max}{}^{2:1\,\Delta t} = \max(d_i{}^{m2:m1})^{M;\Delta t}_{max} - \max(d_j{}^{o2:o1})^{O;\Delta t}_{max} \tag{7}$$

where ~~$o1, o2$ are~~ $d^{O;\Delta t}_{max}$ is computed from observed ice edges at t_0 and $t_0 + \Delta t$ ~~, respectively~~ (black and gray lines in Fig. 1, respectively), and ~~$m1, m2$ are~~ $d^{M;\Delta t}_{max}$ is computed from the corresponding model results. ~~From the results for~~ For the results in the idealized example that was introduced in Sect. 2.1~~above~~ , the model is over-estimating the maximum displacement, by ~~$\Delta d^{2:1}_{max} = 15.3$~~ $\Delta d^{\Delta t}_{max} = 15.3$ grid cell units.

A similar quantity that provides ~~site specific~~ local information is the local difference in displacement of the model ~~binary field where the maximum value is~~ ice edge in proximity of the maximum displacement found in the observations. Let ~~ϵ^{o2}_0~~ $\epsilon^{O;(t_0+\Delta t)}_0$ be the position in ~~$L^{(o2)}$~~ $L^O(t_0+\Delta t)$ to which the maximum edge displacement is found in the observations. Then, determine ~~ϵ^{m2}_0, the~~ $\epsilon^{M;(t_0+\Delta t)}_0$, the model edge grid cell ~~closest position of the model edge~~ positioned closest to $\epsilon^{O;(t_0+\Delta t)}_0$ at the same time. In Fig. 1, the positions ~~ϵ^{o2}_0 and ϵ^{m2}_0~~ $\epsilon^{O;(t_0+\Delta t)}_0$ and $\epsilon^{M;(t_0+\Delta t)}_0$ are indicated by the full black and full red circles, respectively. Following Eq. (3) the corresponding local edge displacement in the model results is

$$\delta_0{}^{m2:m1\,M;\Delta t} = s \min ||\epsilon_0{}^{m2\,M;(t_0+\Delta t)} - L^{(m1)\,M}(t_0)|| \tag{8}$$

~~where $L^{(m1)} = L^{(m)}(t_0)$.~~ For the idealized example, we find that ~~$\delta^{m2:m1}_0 = 83.9$~~ $\delta^{M;\Delta t}_0 = 83.9$. The local difference in displacement between model and observations, with reference to the position ~~ϵ^{o2}_0, becomes~~ $\epsilon^{O(t_0+\Delta t)}_0$, becomes

$$\Delta\delta^{2:1\,\Delta t}{}_{max} = \delta_0{}^{m2:m1\,M;\Delta t} - \max(d_n{}^{o2:o1})^{O;\Delta t}_{max} \tag{9}$$

We recall from Sect. 2.1 that $d^{O;\Delta t}_{max} = 97.9$ so, for the idealized example we have ~~$\Delta\delta^{2:1}_{max} = -14$~~ $\Delta\delta^{\Delta t}_{max} = -14$, *i.e.* a local underestimation of the displacement in the model results.

One aspect which is not disclosed by the metrics introduced thus far, is to what degree forecasts manage to reproduce the geographical location of the observed maximum displacements. In order to examine such a relation, we first compute the decorrelation length of displacements given by Eq. (3). If we denote this grid distance by Δn, we restrict the analysis of grid cells and corresponding displacements to

$$\{\ldots, \epsilon_{0-2\Delta n}{}^{m2\,M}, \epsilon_{0-\Delta n}{}^{m2\,M}, \quad \epsilon_{0+\Delta n}{}^{m2\,M}, \epsilon_{0+2\Delta n}{}^{m2\,M}, \ldots\}(t_0+\Delta t), \tag{10}$$

$$\{\ldots, \delta_{0-2\Delta n}{}^{m2:m1\,M;\Delta t}, \delta_{0-\Delta n}{}^{m2:m1\,M;\Delta t}, \quad \delta_{0+\Delta n}{}^{m2:m1\,M;\Delta t}, \delta_{0+2\Delta n}{}^{m2:m1\,M;\Delta t}, \ldots\} \tag{11}$$

respectively, limited by the first and last ~~nodes~~ cells along the line ~~$L^{(m2)}$~~ $L^M(t_0+\Delta t)$. Next, we construct bins analogously to the method used for producing rank histograms (Talagrand diagrams) for ensemble forecasts ~~(Hamill, 2001)~~ (Hamill, 2001; Talagrand et al., : First, distances listed in Eq. (11) are sorted by increasing values, and then bins are introduced for values smaller than the minimum distance, the intervals between the sorted distances, and for values larger than the maximum distance. The bin placement of ~~$\delta_0^{m2:m1}$~~ $\delta_0^{M;\Delta t}$ then gives the rank of this displacement. A perfect model will have a perfect geographical correspondence between $\delta_0^{M;\Delta t}$ and the position for the maximum displacement in the observations ($d_{max}^{O;\Delta t}$), and all results will belong to the highest (rightmost) bin. A flat histogram indicates a model with no skill, since each bin is equiprobable for random draws.

In the present idealized example we find that $\Delta n = 42$, and the rank of ~~$\delta_0^{m2:m1}$~~ $\delta_0^{M;\Delta t}$ in the 24 resulting bins is 9. When multiple forecasts are examined, the decorrelation length will generally change, as will the length of the edges. Thus, in order to derive a meaningful ~~statistic~~ statistical quantity we subsample a fixed sized random set of grid cells from Eq. (11), and an analysis of the ranks of displacement distances can be performed.

For the idealized example, a set of nine randomly subsampled edge positions from those given by Eq. (10) for the model results at $t = t_0 + \Delta t$ is displayed by open circles in Fig. 1. For this particular case, in the range from 1 to 10 the rank of the displacement ~~$\delta_0^{m2:m1}$~~ $\delta_0^{M;\Delta t}$ is 3.

2.3 ~~Open boundaries and coasts~~

~~Sea ice products may be regional, having one or more boundaries along which the domain is connected to the surrounding area along open ocean boundaries. In that case, sea ice may be advected into the product domain across an open boundary, and the algorithm as given in Sect. 2.1 should be modified in order to avoid misinterpretations of results for displacement distances that may arise. An illustrative case will be discussed in Sect. 3.~~

~~First, set the open boundary grid lines as~~

$$L^{OB} = \{e_{1_{OB}}, e_{2_{OB}}, \ldots, e_{N_{OB}}\}$$

~~where $e_{n_{OB}}$ is any ocean grid cell along the boundary of the domain. Then $L^{(1)}$ can be replaced by~~

$$\tilde{L}^{(1)} = L^{(1)} \cup L^{OB}$$

~~and for the corresponding distances we introduce the notation $\tilde{d}$, so e.g. Eq. (3) is written~~

$$\tilde{d_i}^{2:1} = j \min ||e_i^{(2)} - \tilde{L}^{(1)}||$$

~~It must be noted that if the ice is imported into the domain, the distances $\tilde{d}$ associated with such a displacement will be underestimated, since the real position of the ice edge outside of the analysis domain at t_0 is unknown.~~

~~Similarly, there can be cases where freezing of ice occurs along the coastline, e.g. due to colder air in the vicinity of continents, or less salty water masses close to the coastline. This is another case where the algorithm above can yield grossly exaggerated displacement distances. Again, the problem can be overcome by including additional grid lines.~~

~~Set the coastal grid lines as~~

$$L^{C} = \{e_{1_{C}}, e_{2_{C}}, \ldots, e_{N_{C}}\}$$

~~where e_{n_C} is any ocean grid cell along the coastline. Then $L^{(1)}$ can be replaced by~~

$$\overline{L}^{(1)} = L^{(1)} \cup L^{C}$$

For a regional model, the typical situation is that there are both open boundaries and coastlines. In that case, we may combine the above modifications of the algorithm by adopting

$$\tilde{\bar{L}}^{(1)} = L^{(1)} \cup L^{OB} \cup L^{C}$$

3 A case studyApplication of the new validation method

3.1 Description of sea ice data sets

To illustrate the methodology introduced in Sect. 2, we examine model results from a coupled ocean – sea ice model, and compare with relevant observational data. The model results are taken from the SVIM hindcast archive (SVIM, 2015). For the present illustrative purpose we limit the analysis to the two year period from 1 January 2000 – to 31 December 2001. Results are available as daily means on the model configuration's native 4 km stereographic grid projection (Lien et al., 2013).

The ocean module of the coupled model used for the regional simulation is the Regional Ocean Modeling System (ROMS), described in Haidvogel et al. (2008) and references therein. The sea ice module was developed by Budgell (2005). The ice model dynamics are based on the elastic-viscous-plastic (EVP) rheology after Hunke and Dukowicz (1997) and Hunke (2001), and the ice thermodynamics are based on Mellor and Kantha (1989) and Hakkinen and Mellor (1992).

The model results for sea ice concentration are somewhat noisy on the grid cell scale, owing to the dispersiveness of the numerical scheme. In some regions, the grid cells that constitute the ice edge as defined by Eq. (1) can then appear as a mesh-like collection of cells. In order to reduce the impact of this issue, we applied the second order checkerboard suppression algorithm (Li et al., 2001) to the model results before conducting the present analysis. The sea ice concentrations from observations does not suffer from this type of noise, thus such an algorithm was not applied to the observational data set.

We compare model results with observations from the Arctic Ocean Sea Ice Concentration Charts *Svalbard* which is a multi-sensor product data set that uses data from Synthetic Aperture Radar (SAR) instruments as its primary source of information (WMO, 2017). This product covers observational data set will be referred to as the ice chart data hereafter. The ice chart data cover the northern Nordic Seas, the Barents Sea and adjacent ocean regions. It is available on a stereographic grid projection with a resolution of 1 km. The product will be referred to as the ice chart data hereafter. Data availability is restricted to working days. During a regular week, we then have four days with 24 h displacement results. The data set is also slightly reduced due to holidays, and a total of 354 days with 24 h ice edge displacement results were available from the present two year period.

The present study will be restricted to results and data for the Barents Sea. The SVIM simulation domain is displayed in Fig. 4, where the Barents Sea analysis region is highlighted. Ice chart results are integrated onto the SVIM domain , and all using a mass conserving Riemann integral approach. All grid cells inside the Barents Sea region that become dry in either product which lack proper values (usually due to the presence of land) in at least one of the data sets are masked prior to the analysis. The analysis region is then constituted by 80.399 wet grid cells, which represent an area of $1.29 \cdot 10^{6}$ km^{2}.

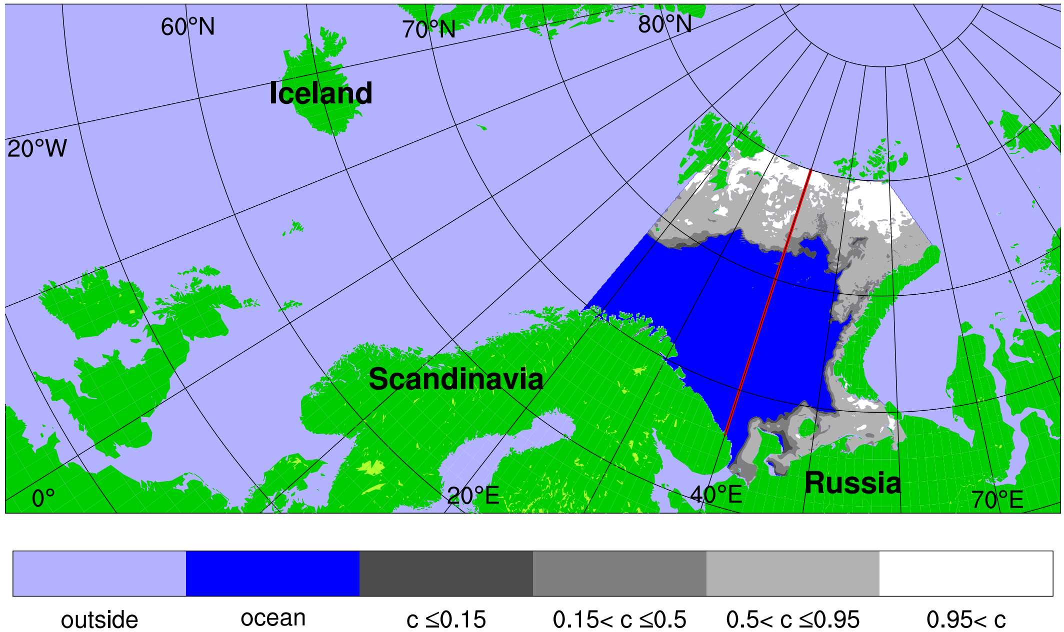

Figure 4. Map of the full SVIM simulation domain. The Barents Sea analysis region in the present study is ~~displayed~~ shown as a highlighted region where a sample sea ice concentration distribution is depicted. The 40°E meridian which will subsequently be used for dividing the domain into two parts, is displayed by the red line. The shading of ice concentration values is given in the label bar, where c is in the sea ice concentration fraction. This sample shows the model results ~~results~~ for 15 April 2000, with the horizontal resolution from the SVIM experiment.

~~Distance General OB & C General OB & C 0 0 0 0 0 – 10 0.06 0.06 0.12 0.12 10 – 20 0.28 0.29 0.06 0.08 20 – 30 0.38 0.38 0.24 0.27 30 – 40 0.17 0.16 0.22 0.21 40 – 50 0.06 0.06 0.15 0.14 50 – 60 0.02 0.02 0.06 0.04 60 – 70 0.01 0.00 0.04 0.04 0.02 0.02 0.11 0.08~~

3.2 Validation results

We first examine the distribution of daily maximum ice edge displacements. ~~The results are summarized in Table ??, where~~ From Fig. 4 we note that this examination will be performed for a domain in which advection of sea ice across the open boundaries is relevant, as well as freezing along coastlines of the continent and archipelagos. Hence, the analysis based on the algorithms in Sect. 2 will be supplemented by the expansion defined by Eq.s (B7)-(B8).

In Fig. 5 results from the 354 days with 24 h maximum displacements from both ~~products have been included~~data sets are displayed. We note that about 2/3 of the maximum displacements in model results are in the range 10 – 30 km. The corresponding distribution of results from the ice chart data has two maxima, one for the range 20 – 40 km which accounts for nearly half of the cases, and a secondary maximum for short (0 – 10 km) maximum displacements. The averages of the daily maximum displacement distances are 25 km and 36 km for the SVIM results and the ice chart data, respectively.

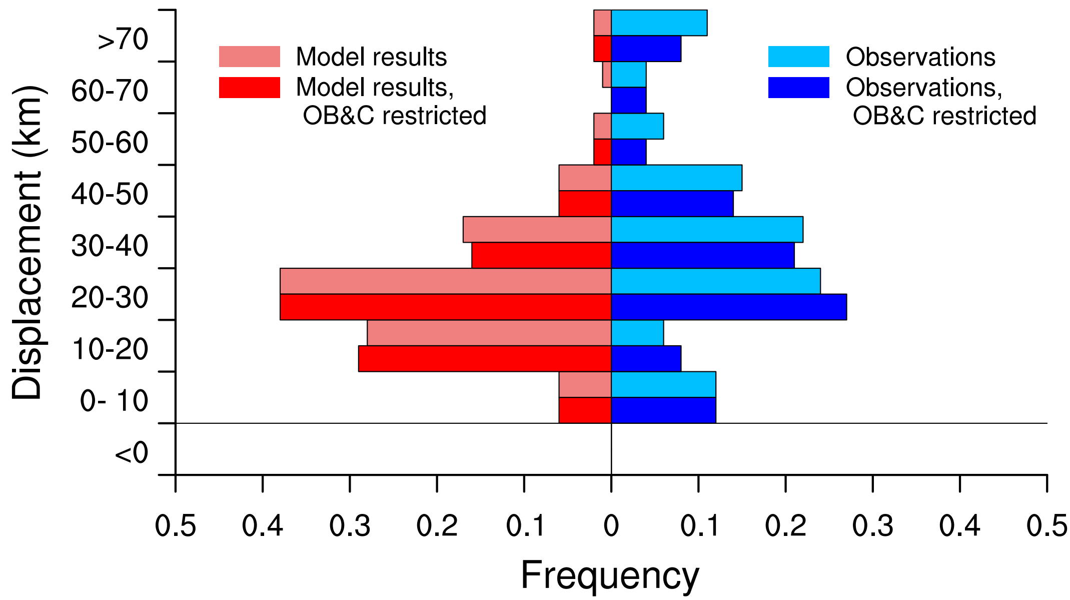

Figure 5. ~~Category distribution~~ Histograms for ~~ice edge displacement distances. Leftmost column gives~~ the distribution of daily maximum displacement ~~distance range for each category~~distances $\Delta d^{\Delta t}_{max}$, ~~in km~~defined by Eq.~~Results~~ (5). Horizontal bars pointing left and right correspond to results from SVIM model simulation and ice chart data~~are presented separately~~, respectively. ~~Fractions in columns “General” are computed~~ Light colored bars display results from ~~Eq~~the original algorithm in Sect. ~~(3)~~2.1, while ~~fractions in columns~~ bars with regular colors (labeled “OB&C restricted”~~also take displacements from~~) result after the extension in Appendix B for open boundaries and ~~coasts into account, by replacing $L^{(1)}$ with $\tilde{\tilde{L}}^{(1)}$ as defined by Eq. (B7)~~coastlines is applied. Results from 354 days of 24h edge displacements have been analyzed, see the text for further details.

A conclusion that can be drawn from these results is that the largest expansions of sea ice extent in the model (SVIM) result are underestimations when compared with observations (ice chart data). This is generally the case, as the SVIM median is in the range 20 – 30 km, while the median of the ice chart data is in the range 30 – 40 km. The underestimation is also seen for extreme cases, as the frequency of maximum expansion exceeding 60 km is about five times as high for the ice chart data. Note that the ice chart data deviates from passive microwave products, particularly in the final months of the melting season (e.g. Sect. 6 in Melsom et al. (2019)). Hence, the true sea ice extent is unknown.

The ~~category distributions in Table ?? change~~ distribution frequencies in Fig. 5 changes only moderately when ~~the algorithm for computing displacements are modified~~ including open ocean boundaries and coastal lines as described in ~~Sect. ??~~Appendix B. However, in a few cases the results from the general algorithm given in Sect. 2.1 do not properly describe true displacements. To illustrate this, we have selected a case where the two approaches give diverging results: the change in the ice edge position from 23 October 2001 to 24 October 2001, as displayed in Fig. 6.

This is a case where sea ice is displaced into the analysis region across the ~~northern boundary~~ open boundary in the north. The example demonstrates that in such cases, the general algorithm in Sect. 2.1 ~~gives unreasonable results~~mis-matches ice edge

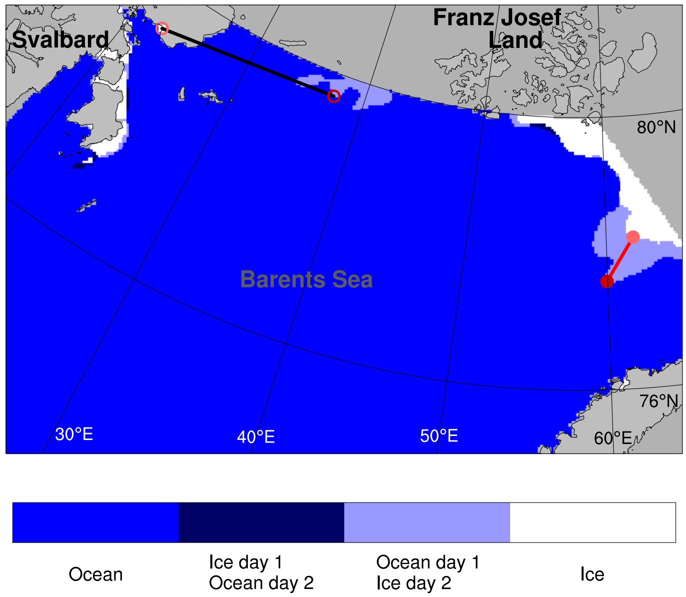

Figure 6. Sample scene displaying the changes in model sea ice extent from 23 October 2001 (day 1) to 24 October 2001 (day 2). The black line indicates the maximum displacement distance ($d^{2:1}_{max}$$d^{\Delta t}_{max}$, given by Eq. (5) with the original algorithm, while the red line shows the result when grid nodes cells along the open boundaries and coastlines are included ($\tilde{\tilde{L}}^{(1)}$ $\tilde{\tilde{L}}(t_0)$ from Eq. (B7))). The color coding is given by the label bar, and note that only the northern part of the Barents Sea analysis region is displayed.

grid cells: The maximum displacement of 285 km that emerges from the algorithm is indicated by a black line. The maximum distance using the modified algorithm in Sect. ?? Appendix B is 79 km (red line).

For the examination of In order to examine the degree to which SVIM results reproduce the geographical location of the observed maximum displacement, nine values were chosen randomly from we apply the ranking method described in Sect. 2.2. We will use a rank size of ten for the present investigation. Hence, for each set of 24 h results for displacement distances, nine values will be chosen randomly from the results emanating from Eq. (s (8) and (11). Moreover, the requirement of at least nine additional ice edge positions separated by the decorrelation length scale restricts the cases that can be considered in this analysis. Thus, from From the full set of 354 cases with 24 h displacement results, 235 cases were could then be kept in the analysis of ranked displacements, as these cases met the requirement of at least 10 statistically independent displacement distances. The size of the set of independent values is restricted by the temporally varying degrees of freedom, as given by the fraction of the ice edge length and the decorrelation length scale.

The resulting frequency distribution for each of the ten ranks is displayed as gray vertical bars in Fig. 7(a), with rank values from 0 to 9. The highest rank (9) results when the model displacement close to the site with maximum displacement in the observations (the reference displacement, $\delta_0^{m2:m1}$$\delta_0^{M;\Delta t}$) is larger than all displacements from the nine subsampled ice edge positions. The next rank (8) corresponds to cases where one and only one of the subsampled positions have a larger

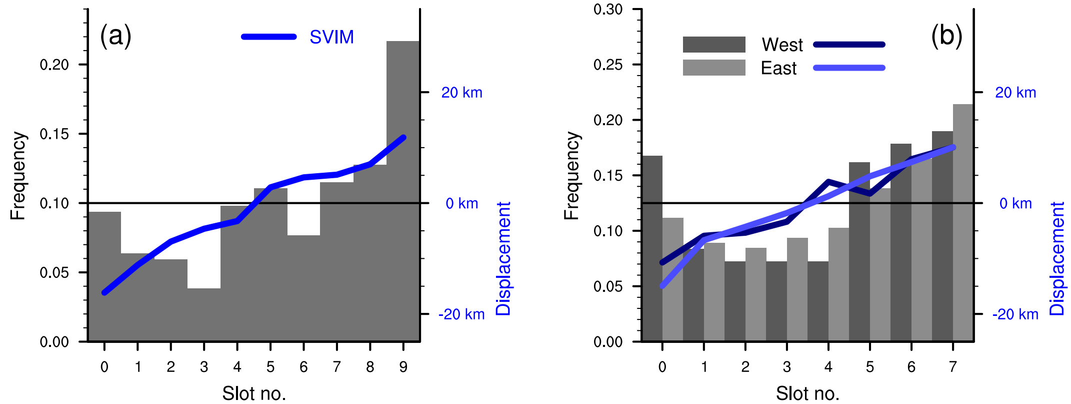

Figure 7. Rank histogram for model results for the local ice edge displacement corresponding to the position of the maximum observed displacement. (a): Sets of nine alternative model displacements were derived for each of 235 days with 24 h displacements results. The nine displacement values were ordered from lowest to highest, and the local displacement was given a rank from the slot in which this value ~~belongs~~belonged, see the text for details. The ~~black~~ blue curve shows the average local model displacement distances for results belonging to each of the ranks, with negative numbers corresponding to local sea ice retreat in the model results. The average maximum observed displacement is ~~32~~39 km. (b): Results obtained for a subdivision as indicated by the red line in Fig. 4. Here, sets of seven alternative displacements results were derived for each subdomain. Then, results were available for 179 days and 224 days for the western and eastern subdomain, respectively. The average maximum observed displacements are 36 km in both subdomains. The use of gray shading and line colors for the subdomains are indicated by the inset label.

displacement than the reference displacement, and so on. In other words, high ranks indicate situations in which the position of the maximum displacement is described with a relatively high quality.

~~The expected average rank from~~ Note that the axes indicating displacements of 0 km in Fig. 7(a),(b) have been positioned to indicate the flat distribution of rank frequencies that is expected for a model with no ~~quality in reproducing the position of the maximum ice edge displacement is 4.5, with half of the cases with arank in the range 0~~skill.

The histogram in Fig. 7(a) has nearly twice as many entries in ranks 5 – ~~4, and the other half in the range 5~~9 as ranks 0 – ~~9. In the analysis of the~~ 4. This mode for higher ranks indicate some skill for results from the SVIM archive ~~, we find that 35% of the cases have rankings in the range 0 – 4, while 65% have rankings in the range 5 – 9.~~

in detecting the location of the maximum displacements in the observations. Furthermore, the average rank in the present analysis is ~~5.5~~5.48. For a random distribution of 235 integer numbers in the range 0 –9 the ~~0.005th and 0.995th percentiles are 4.015 and 4.985~~0.5th and 99.5th percentiles of the average rank are 4.02 and 4.98, respectively. Thus, the analysis reveals that while the model results are far from perfect, the average ~~ranking of 5.5~~ rank of 5.48 is significantly higher than results from random spatial distributions of ice edge displacements. See Wilks (2019) for a more comprehensive analysis of the flatness of rank histograms.

We supplement this analysis by dividing the region into two subdomains, separated by the 40°E meridian, as indicated by the red line in Fig. 4. In order to retain the majority of the days in the analysis, the number of randomly chosen displacements was reduced to seven values. This was due to the reduced degrees of freedom when the same decorrelation length scale was applied in smaller domains, with shorter ice edges.

The results for the eastern and western Barents Sea subdomains are displayed in Fig. 7(b). The average ranks of the model displacements corresponding to the largest observed displacements are 3.95 and 4.13 in the western and eastern subdomain, respectively. The ranges spanned between the 0.5^{th} and 99.5^{th} percentiles for random distributions become [3.06,3.94] and [3.11,3.89] for the western (179 days) and eastern (224 days) subdomain, respectively.

4 Concluding remarks

We present a simple algorithm for examination of the displacement of the edge (or the front) of a binary field. This forms the basis for a subsequent analysis of , from which statistical properties for such displacementsdisplacement distances can be inferred. Furthermore, additional methods have been introduced for the purpose of comparing two different products that are available as descriptions of the same situationdata sets. These methods are e.g. relevant when assessing the quality of forecasted displacements of the edge. The results from these methods expand on existing validation metrics such as e.g. the Integrated Ice-Edge Error (Goessling et al., 2016) and the various ice edge metrics considered by Melsom et al. (2019): The present methods provide summary statistics for the quality of model results for ice edge displacements in the presence of an expanding sea ice cover, as exemplified by Fig. 5 and Fig. 7, that are not provided with existing metrics. Such quality assessments are of high relevance for planned or ongoing site specific activities in regions which can potentially become ice infested.

The present study has been framed in the context of results for displacements of the sea ice edge. Thus, the case study which was investigated investigation in Sect. 3 was based on data for the sea ice edge from satellite observations, and simulation results from a coupled ocean – sea ice model. However, the algorithm that was introduced in Sect. 2 can be applied to the displacement of the perimeter of any property that can be represented by a continuous binary field. Stratiform precipitation is an example of another property for which the present methods are relevant.

Note that we have used the term *displacement* rather than *advection*. The reason for this is that displacements need not be purely of an advective nature. In the case of sea ice, the displacement of the initial edge will generally be affected by freezing or melting along the perimeter of the sea ice extent. Analogously, displacement of the area affected by stratiform precipitation can be affected by new condensation or partial depletion of the cloud.

As demonstrated in the example depicted in Fig. 6, the original algorithm described in Sect. 2.1 and 2.2 may yield results that represent other aspects than true displacements. Here, we have amended situations in which the sea ice enters a limited area domain across an open model domain boundary, and situations where freezing takes place next to a physical boundary (the coast). The corresponding simple modifications of the algorithm that was introduced in Sect. ?? is introduced in Appendix B eliminates such issues, as revealed from the sample situation in Fig. 6.

However, there may be other issues that can distort results that are produced by the present analysis. One example is cases where features are seen to arise seemingly spontaneous from one time of analysis to another: The algorithm in Sect. 2 can e.g., if applied to precipitation data, give rise to unrealistic results for displacements when convective precipitation cells become establisheddevelop.

Results from the algorithms that are introduced in the present study give valuable information regarding the changing extent of sea ice, and how well the displacement displacements of the observed and modeled sea ice edge edges agree. These algorithms have proven to provide simple, yet robust and informative assessments for the quality of ice edge forecasts both with respect to the largest displacements from one time to another as well as with respect to the reproduction of the geographical position where the largest displacement occurs.

Code and data availability. The idealized distributions of concentrations that are depicted in Fig. 1, and source code for computing results displayed in Fig. 2 and Fig. 3, are available from https://doi.org/10.5281/zenodo.4545686 (Melsom, 2021). Model results that were analyzed in Sect. 3 are available from https://archive.norstore.no/pages/public/datasetDetail.jsf?id=10.11582/2015.00014 (SVIM, 2015), while the observations are available from https://thredds.met.no/thredds/catalog/arcticdata/met.no/iceChartSat/catalog.html.

Appendix A: Decorrelation length of displacements

Assume that a we have a set of N edge grid cells e_n (i.e. satisfying Eq. (1)) that form a line

$$L = \{e_1, e_2, \ldots, e_N\} \tag{A1}$$

where L is continuous in the sense that grid cells e_n and e_{n+1} are neighbors. Furthermore, associate displacement distances d_n to each e_n as defined in Sect. 2.1. Then, the spatial autocorrelation of displacements can be estimated using a sample Pearson correlation coefficient approach:

$$r(\eta) = \sum_{n=1}^{N-\eta} \left[(d_n - \overline{d_n})(d_{n+\eta} - \overline{d_{n+\eta}})\right] \Bigg/ \left[\sum_{n=1}^{N-\eta} (d_n - \overline{d_n})^2 \sum_{n=1}^{N-\eta} (d_{n+\eta} - \overline{d_{n+\eta}})^2\right]^{1/2} \tag{A2}$$

We have $r(0) = 1$ and we define the decorrelation length of the displacements, Δn, as

$$\Delta n = \min_{\forall \eta}(\eta \mid r(\eta) < 1/\mathrm{e}\,) \tag{A3}$$

where e is Euler's number. If, for a given time, the ice edge is discontinuous, each continuous line segment is treated separately, and the weighted mean value of the results for Δn from each segment is used. In that case, weights are applied according to the number of edge grid cells in each line segment.

Appendix B: Open boundaries and coasts

As discussed by Melsom et al. (2019), open boundaries and coastlines can potentially have significant impacts on the results for the metrics for the position of the sea ice edge. Here, we introduce a method which will give more physical meaningful

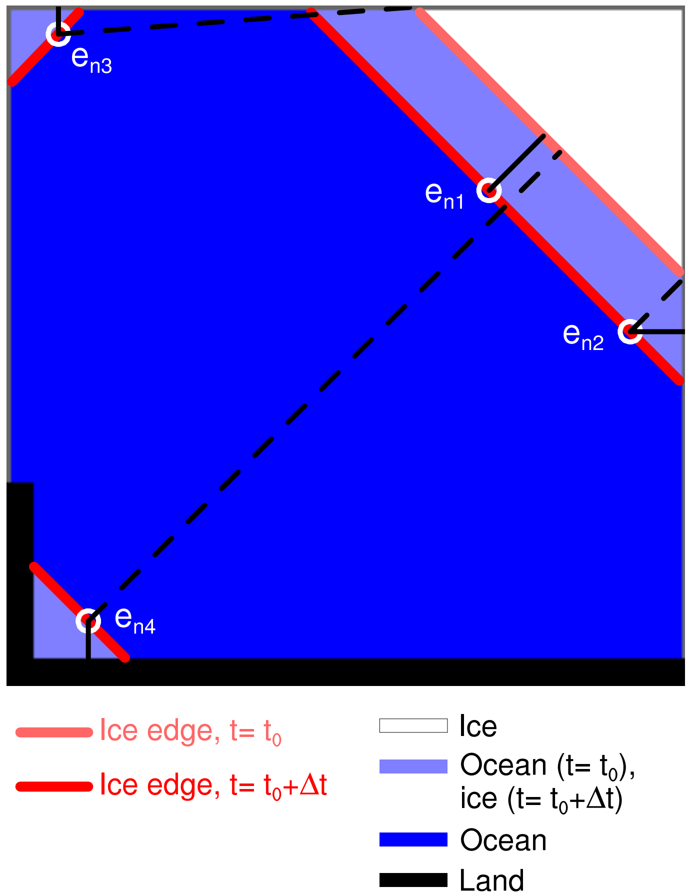

Figure B1. Binary fields with values of 1 (ice) and 0 (no ice/ocean) are displayed by white and blue color shading, respectively. Land is indicated as a black region. Light shades of blue indicate regions with a non-overlapping ice cover, as indicated by the inset color legend. Open boundary grid cells are depicted as gray lines. Ice edges for t_0 and $t_0+\Delta t$ are drawn as light red and red and lines, respectively. Dashed black lines show the edge displacements as defined in Sect. 2.1, for a selection of labeled ice edge grid cells from $t_0+\Delta t$, marked by white circles. Full black lines display the displacements $\tilde{\tilde{d}}$ that result from the modifications described in Appendix B, see Eq. (B8). For the set of grid cells that are highlighted here, only e_{n1} is unaffected by the modified definitions.

results if ice either freezes near a coastline, or enters into a domain across an open boundary. Moreover, the method affects the results modestly or not at all for an edge that is displaced inside of the domain.

First, set the open boundary grid lines to

$$L^{OB}(t_0)=\{e_{1_{OB}},e_{2_{OB}},\ldots,e_{N_{OB}}\} \quad , \quad c[e_{n_{OB}}](t_0)<c_{edge} \tag{B1}$$

where $e_{n_{OB}}$ is any ocean grid cell along the boundary of the domain which was on the open ocean side of the ice edge at $t = t_0$. Then $L(t_0)$ in Eq. (3) can be replaced by

$$\widetilde{L}(t_0) = L(t_0) \cup L^{OB}(t_0) \quad \text{(B2)}$$

and for the corresponding distances we introduce the notation $\widetilde{d}$, so Eq. (3) becomes

$$\widetilde{d_n}^{\Delta t} = \min ||e_n^{(t_0+\Delta t)} - \widetilde{L}(t_0)|| \quad \text{(B3)}$$

where $e_n^{(t_0+\Delta t)}$ is a grid cell on $L(t_0 + \Delta t)$, as before. Note that the set of grid cells $e_n^{(t_0+\Delta t)}$ is not affected, so the number of displacement distances considered in Eq. (5), $N(t_0 + \Delta t)$, is unchanged.

A sample grid cell to which the displacement distance is significantly affected by this modification, is displayed as e_{n3} in Fig. B1. It must be noted that if the ice is imported into the domain, the distances $\widetilde{d}$ associated with such a displacement will be underestimated, since the real position of the ice edge outside of the analysis domain at t_0 is unknown. Moreover, for regular displacement of ice inside the domain, results will be affected slightly when occurring in the vicinity of the open boundary (e.g. e_{n2} in Fig. B1).

Similarly, there can be cases where freezing of ice occurs along the coastline, e.g. as an effect of colder air in the vicinity of continents, or less salty water masses close to the coastline. This is another case where the algorithm above can yield grossly exaggerated displacement distances. Again, the problem can be alleviated by including additional grid lines.

Set the coastal grid lines as

$$L^C(t_0) = \{e_{1_C}, e_{2_C}, \ldots, e_{N_C}\} \quad , \quad c[e_{n_C}](t_0) < c_{edge} \quad \text{(B4)}$$

where e_{n_C} is any ocean grid cell along the coastline which was ice free or had a sea ice concentration below c_{edge} at $t = t_0$. Then $L(t_0)$ can be replaced by

$$\overline{L}(t_0) = L(t_0) \cup L^C(t_0) \quad \text{(B5)}$$

Here, Eq. (3) will be replaced by

$$\overline{d_n}^{\Delta t} = \min ||e_n^{(t_0+\Delta t)} - \overline{L}(t_0)|| \quad \text{(B6)}$$

and the computation of the displacement distance to grid cell e_{n4} in Fig. B1 is severely affected.

For a regional model, the typical situation is that there are both open boundaries and coastlines. In that case, we may combine the above modifications of the algorithm by adopting

$$\widetilde{\overline{L}}(t_0) = L(t_0) \cup L^{OB}(t_0) \cup L^C(t_0) \quad \text{(B7)}$$

and Eq. (3) can be written

$$\widetilde{\overline{d_n}}^{\Delta t} = \min ||e_n^{(t_0+\Delta t)} - \widetilde{\overline{L}}(t_0)|| \quad \text{(B8)}$$

Author contributions. Melsom performed the analysis in its entirety, produced all figures and wrote the article.

Competing interests. The author declares that he has no conflict of interest.

Acknowledgements. This study was performed within the Nansen Legacy project on behalf of the Norwegian Research Council, funded under contract no. 276730. Supporting funding was provided by the Copernicus Marine Environmental and Monitoring Service under Mercator Océan from contract no. 2015/S 009-011301. Yvonne Gusdal is acknowledged for performing the hindcast simulation. All figures were made using the NCAR Command Language (NCL, 2017). Referee comments from two anonymous reviewers were especially helpful during the revision of this article. I am very grateful for the reviewers' efforts.

References

Aksenov, Y., Popova, E. E., Yool, A., Nurser, A. G., Williams, T. D., and Bertino, L.: On the future navigability of Arctic sea routes: High-resolution projections of the Arctic Ocean and sea ice, Mar. Policy, 75, 300-317, doi:10.1016/j.marpol.2015.12.027, 2017.

Anderson, J. L., A method for producing and evaluating probabilistic forecasts from ensemble model integrations, J. Climate, 9(7), 1518-1530, doi:10.1175/1520-0442(1996)009<1518:AMFPAE>2.0.CO;2, 1996.

Bitz, C. M., Holland, M. M., and Hunke, E. C.: Maintenance of the Sea-Ice Edge J. ~~Clim.~~Climate, 18(15), 2903-2921, doi:10.1175/JCLI3428.1, 2005.

Budgell, P. W.: Numerical simulation of ice-ocean variability in the Barents Sea region: Towards dynamical downscaling, Ocean ~~Dyn~~Dynam., 55(3-4), 370-387, doi:10.1007/s10236-005-0008-3, 2005.

Cheng, A., Casati, B., Tivy, A., Zagon, T., and Lemieux, J. F.: Accuracy and inter-analyst agreement of visually estimated sea ice concentrations in Canadian Ice Service ice charts using single-polarization RADARSAT-2, The Cryosphere, 14, 1289-1310, doi:10.5194/tc-14-1289-2020, 2020.

Davis, C. A., Brown, B. G., and Bullock, R. G.: Object-based verification of precipitation forecasts, Part I: Methodology and application to mesoscale rain areas, Mon. Weather Rev. 134(7), 1772-1784, doi:10.1175/MWR3145.1, 2006.

Dukhovskoy, D. S., Ubnoske, J., Blanchard-Wrigglesworth, E. , Hiester, H. R., and Proshutinsky, A.: Skill metrics for evaluation and comparison of sea ice models, J. Geophys. Res. Oceans, 120, 5910-5931, doi:10.1002/2015JC010989, 2015.

Ebert, E. E., and McBride, J. L.: Verification of precipitation in weather systems: determination of systematic errors, J. Hydrol., 239, 179-202, doi:10.1016/S0022-1694(00)00343-7, 2000.

Goessling, H. F., and Jung, T.: A probabilistic verification score for contours: Methodology and application to Arctic ice-edge forecast, Q. J. Roy. Meteor. Soc., 144, 735–743, doi:10.1002/qj.3242, 2018.

Goessling, H. F., Tietsche, S., Day, J. J., Hawkins, E., and Jung, T.: Predictability of the Arctic sea ice edge, Geophys. Res. Lett., 43, 1642-1650, doi:10.1002/2015GL067232, 2016.

~~Goessling, H. F., and Jung, T.: A probabilistic verification score for contours: Methodology and application to Arctic ice-edge forecast, Q. J. R. Meteorol. Soc., 144, 735–743, doi:10.1002/qj.3242, 2018.~~

Haidvogel, D. B., Arango, H. G., Budgell, P. W., and 17 coauthors: Ocean forecasting in terrain-following coordinates: Formulation and skill assessment of the Regional Ocean Modeling System, J. ~~Comp~~Comput. Phys., 227(7), 3595-3624, doi:10.1016/j.jcp.2007.06.016, 2008.

Häkkinen, S., and Mellor, G. L.: Modelling the seasonal variability of a coupled arctic ice-ocean system, J. Geophys. Res., 97(C12), 20.285-20.304, doi:10.1029/92JC02037, 1992.

Hamill, T. M.: Interpretation of Rank Histograms for Verifying Ensemble Forecasts, Mon. ~~Wea.~~ Weather Rev., 129(3), 550-560, doi:10.1175/1520-0493(2001)129<0550:IORHFV>2.0.CO;2, 2001.

Hunke, E. C.: Viscous-plastic sea ice dynamics with the EVP model: linearization issues, J. Comput. Phys., 170, 18-38, doi:10.1006/jcph.2001.6710, 2001.

Hunke, E. C. and Dukowicz, J. K.: An elastic-viscous-plastic model for sea ice dynamics, J. Phys. Oceanogr., 27, 1849-1867, doi:10.1175/1520-0485(1997)027<1849:AEVPMF>2.0.CO;2, 1997.

Lavergne, T., Eastwood, S., Teffah, Z., and Schyberg, H.: Sea ice motion from low-resolution satellite sensors: An alternative method and its validation in the Arctic, J. Geophys. Res., 115, C10032, doi:10.1029/2009JC005958, 2010.

Leese, J. A., Novak, C. S., and Clark, B. B.: An Automated Technique for Obtaining Cloud Motion from Geosynchronous Satellite Data Using Cross Correlation, J. Appl. Meteorol., 10(1), 118-132, doi:10.1175/1520-0450(1971)010<0118:AATFOC>2.0.CO;2, 1971.

Li, Q., Steven, G. P., and Xie, Y. M.: A simple checkerboard suppression algorithm for evolutionary structural optimization, Struct. ~~Optim.~~Optimization, 22(3), 230-239, doi:10.1007/s001580100140, 2001.

Lien, V. S., Gusdal, Y., Albretsen, J., Melsom, A., and Vikebø, F. B.: Evaluation of a Nordic Seas 4 km numerical ocean model hindcast archive (SVIM), Fisken og Havet, 2013-7, 80pp, 2011.

Mellor, G. L., and Kantha, L.: An ice-ocean coupled model, J. Geophys. Res., 94(C8), 10.937-10.954, doi:10.1029/JC094iC08p10937, 1989.

Melsom, A.: Edge metrics software v.1.0 [Software], Zenodo, doi:10.5281/zenodo.4545686, 2021.

Melsom, A., Palerme, C., and Müller, M.: Validation metrics for ice edge position forecasts, Ocean ~~Science~~Sci., 15(3), 615-630, doi:10.5194/os-15-615-2019, 2019.

The NCAR Command Language (Version 6.4.0) [Software], Boulder, Colorado: UCAR/NCAR/CISL/TDD, doi:10.5065/D6WD3XH5, 2017.

Norwegian Meteorological Institute, Institute of Marine Research: SVIM ocean hindcast archive [Data set], National Infrastructure for Research Data, doi:10.11582/2015.00014, 2015.

Palerme, C., Müller, M., and Melsom, A.: An intercomparison of skill scores for evaluating the sea ice edge position in seasonal forecasts, Geophys. Res. Lett., doi:10.1029/2019GL082482 (accepted for publication), 2019.

Parkinson, C. L.: Spatially mapped reductions in the length of the Arctic sea ice season, Geophys. Res. Lett., 41(12), 4316-4322, doi:10.1002/2014GL060434, 2014.

Talagrand, O., Vautard R., and Strauss B.: Evaluation of probabilistic prediction systems, Proc. Workshop on Predictability, ECMWF, Reading, United Kingdom, 20-22 October 1997, 25pp, 1997.

Tokmakian, R., Strub, P. T., and McClean-Padman, J.: Evaluation of the Maximum Cross-Correlation Method of Estimating Sea Surface Velocities from Sequential Satellite Images, J. Atmos. Ocean. Tech., 7(6), 852-865, doi:10.1175/1520-0426(1990)007<0852:EOTMCC>2.0.CO;2, 1990.

Wilks, D.: Indices of Rank Histogram Flatness and Their Sampling Properties, Mon. Weather Rev., 147(2): 763-769, doi:10.1175/MWR-D-18-0369.1, 2019.

WMO: Sea-Ice Information Services in the World, ~~WMO~~ World Meteo. No. 574, World Meteorological Organization, 103pp, 2017.